ЖЭТФ, 2013, том 143, вып. 2, стр. 271–287

STUDIES OF CONCENTRATION AND TEMPERATURE DEPENDENCES OF PRECIPITATION KINETICS IN IRON–COPPER ALLOYS USING KINETIC MONTE CARLO AND STOCHASTIC STATISTICAL SIMULATIONS

K. Yu. Khromov, V. G. Vaks**, I. A. Zhuravlev

National Research Center "Kurchatov Institute"
123182, Moscow, Russia

Moscow Institute of Physics and Technology
141700, Moscow, Russia

Received June 13, 2012

The previously developed *ab initio* model and the kinetic Monte Carlo method (KMCM) are used to simulate precipitation in a number of iron–copper alloys with different copper concentrations x and temperatures T. The same simulations are also made using an improved version of the previously suggested stochastic statistical method (SSM). The results obtained enable us to make a number of general conclusions about the dependences of the decomposition kinetics in Fe–Cu alloys on x and T. We also show that the SSM usually describes the precipitation kinetics in good agreement with the KMCM, and using the SSM in conjunction with the KMCM allows extending the KMC simulations to the longer evolution times. The results of simulations seem to agree with available experimental data for Fe–Cu alloys within statistical errors of simulations and the scatter of experimental results. Comparison of simulation results with experiments for some multicomponent Fe–Cu-based alloys allows making certain conclusions about the influence of alloying elements in these alloys on the precipitation kinetics at different stages of evolution.

DOI: 10.7868/S0044451013020077

1. INTRODUCTION

Studies of the composition and temperature dependences of the precipitation kinetics in alloys, in particular, in the multicomponent Fe–Cu-based steels used in many industrial applications, attract great attention [1–11]. For such studies, it seems to be useful to have a reliable information about similar dependences for simpler, binary alloys treated as reference systems. For example, discussing the precipitation kinetics in two Fe–Cu-based steels, NUCu-140 and NUCu-170, the authors of [5, 6] compared their experimental results with those for several Fe–xCu binaries with x between 1.34 and 1.5 at. %, while the two steels considered had notably different content of copper, 1.17 and 1.82 %, respectively. Because many characteristics of nucleation and growth, in particular, sizes and density of precipitates, strongly vary with $x = x_{\mathrm{Cu}}$, such a comparison is not necessarily correct. The precipitation characteristics can also significantly depend on temperature, while measurements of such dependences, for the nucleation stage in particular, often meet difficulties [5, 6].

To obtain quantitative information about the precipitation kinetics, particularly in the course of nucleation and growth, one can use simulations of these processes, if both the microscopic model and the simulation methods can be considered reliable. For the Fe–Cu alloys, such a reliable *ab initio* model has been developed by Soisson and Fu [9], and their detailed kinetic Monte Carlo simulations of nucleation and growth in the Fe–1.34Cu alloy at $T = 773$ K revealed good agreement with the available experimental data.

The first aim of this work is therefore to use the model and the kinetic Monte Carlo method (KMCM) developed in [9] to study the concentration and temperature dependences of the precipitation kinetics in binary Fe–Cu alloys for several copper concentrations

*E-mail: vaks@mbslab.kiae.ru

x and temperatures T, including those used in [5, 6] for the NUCu steels. Comparing results of these simulations to the available experimental data allows assessing the reliability of Soisson and Fu's model at different x and T and also discussing the differences in the precipitation kinetics between the Fe–xCu binaries and multicomponent Fe–Cu-based alloys with the same $x = x_{\mathrm{Cu}}$ and T.

The second aim of this work is to discuss possible applications of the previously suggested stochastic statistical method (SSM) [13] for simulations of precipitation kinetics in those cases where the KMCM encounters difficulties. Such difficulties arise, for example, in treating the coarsening stage or at relatively low temperatures $T \lesssim 300\,^{\circ}\mathrm{C}$ (typical for service of many nuclear reactors) when the KMC simulations become time consuming [9, 10]. Unlike the KMCM, the SSM allows parallelizing computer codes, which can greatly accelerate computations, and this method seems to be also suitable for various generalizations, for example, for considerations of lattice misfit effects. However, in treatments of nucleation, some oversimplified models were used in Ref. [13], which resulted in some fictitious breaks in the simulated temporal dependences. In this work, we describe an improved version of the SSM, which is free from these shortcomings, and show that this version describes the main characteristics of nucleation, including the density and sizes of precipitates, in good agreement with the KMCM. We also show that using the SSM in conjunction with the KMCM allows extending the KMC simulations to the first stages of coarsening.

In Sec. 2, we briefly discuss the model, the alloy states, and the methods used in our simulations. In Sec. 3, we describe the improved version of the SSM. The results of our simulations are discussed and compared with the available experimental data in Sec. 4. The main conclusions are given in Sec. 5.

2. MODELS AND METHODS OF SIMULATIONS

For our simulations, we use the *ab initio* model of Fe–Cu alloys developed by Soisson and Fu and described in detail in Refs. [9, 10, 13]. Here, we only note that this model uses the following values of the binding energy between two copper atoms and between a copper atom and a vacancy, E^{bn}_{CuCu} and $E^{bn}_{\mathrm{Cu}v}$, for the nth nearest neighbors (in eV):

$$\begin{aligned} E^{b1}_{\mathrm{CuCu}} &= 0.121 - 0.182T, \\ E^{b2}_{\mathrm{CuCu}} &= 0.021 - 0.091T, \\ E^{b1}_{\mathrm{Cu}v} &= 0.126, \quad E^{b2}_{\mathrm{Cu}v} = 0.139. \end{aligned} \tag{1}$$

The high values of E^{bn}_{CuCu} correspond to the strong thermodynamic driving force for precipitation, while the strong attraction of a vacancy to copper atoms results in strong vacancy trapping by copper precipitates, discussed in detail in [9].

The alloy states (below, *states* for brevity) used in our simulations are listed in Table 1. The degree of supersaturation for each of these states is characterized by the reduced supersaturation parameter s introduced in Refs. [13, 14]:

$$s(x,T) = [x - x_b(T)]/[x_s(T) - x_b(T)], \tag{2}$$

where the subscript s or b corresponds to a spinodal or a binodal. Values $s < 1$ correspond to the nucleation and growth evolution type, and $s > 1$, to spinodal decomposition.

The states A and C in Table 1 have the same temperature T and the copper content x as the steels NUCu-140 and NUCu-170 studied in [5, 6]. For the states B and G, kinetics of precipitation under thermal aging was investigated experimentally in [1–3, 7], while for the state F, precipitation under neutron irradiation was studied in [4]. For the states D and E, experimental data about the precipitation kinetics are not known to us, and our simulations are made to study its temperature dependence.

In Table 1, we also present some parameters of the "thermodynamic" critical embryos for the states considered: the nucleation barrier F_c, the total number N_c^{th} of copper atoms within an embryo, and the critical radius R_c^{th} defined as the radius of the sphere having the same volume as N_c^{th} copper atoms in the BCC lattice of α-iron with the lattice constant $a = 0.288$ nm:

$$R_c^{th} = a(3N_c^{th}/8\pi)^{1/3} = 0.142\,(N_c^{th})^{1/3}\,\mathrm{nm}. \tag{3}$$

The characteristics of critical embryos shown in Table 1 and Fig. 1 are calculated by the statistical method of Dobretsov and Vaks [14] with the use of the *ab initio* model by Soisson and Fu [9] and the pair cluster approximation, which is typically highly accurate, particularly for dilute alloys, as both analytic studies [15] and comparisons with Monte Carlo simulations [16] show. Table 1 and Fig. 1 illustrate, in particular, a decrease in the nucleation barrier F_c and the embryo size N_c^{th} as the supersaturation s increases. Table 1 also shows that for a given supersaturation s, decreasing the temperature T affects the critical embryo characteristics

Table 1. The Fe–xCu alloy states considered and parameters of "thermodynamic" critical embryos for these states calculated by the method in Ref. [14]

Alloy state	T, K	x, at. %	s	F_c/T	N_c^{th}	R_c^{th}, nm
A	773	1.17	0.247	5.58	15.4	0.353
B	773	1.34	0.285	4.38	14.3	0.344
C	773	1.82	0.393	2.30	12.2	0.326
D	713	1.34	0.352	2.47	10.7	0.312
E	663	1.34	0.425	1.36	8.2	0.286
F	561	0.78	0.387	1.11	5.3	0.247
G	873	1.15	0.163	12.6	28.3	0.433

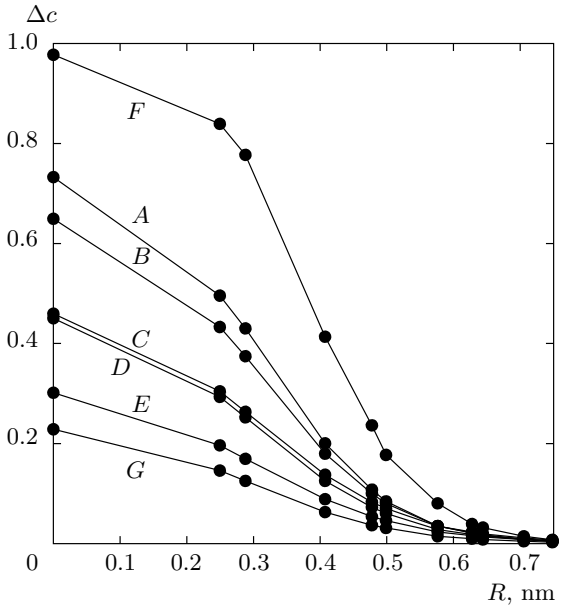

Fig. 1. Concentration profiles $\Delta c(R) = c(R) - x$ in thermodynamic critical embryos for the alloy states considered, where $c(R) = c_{\mathrm{Cu}}(r)$ is the mean copper concentration at the distance R from the embryo center

stronger than increasing the concentration x [13]. As discussed below, the N_c^{th} and R_c^{th} values presented in Table 1 are usually close to those estimated in KMC simulations and in experiments.

The methods of both KMC and SSM simulations used in this work are described in detail in Refs. [9, 13]. Here, we only mention some details of computations. For both the KMC and the SSM simulations, we typically used the simulation volume $V_s = (64a)^3$; for the state G with low supersaturation, we used the larger value $V_s = (128a)^3$. In our KMC simulations, we usually followed $N_s^{KMC} \sim 10^{13}$ Monte Carlo steps, which at $V_s = (64a)^3$ took about five months on a standard workstation. The SSM simulations for $V_s = (64a)^3$ took usually about a month on a standard workstation (with no parallelization of codes made).

3. IMPROVEMENTS OF STOCHASTIC STATISTICAL METHOD

The original version of the SSM is described in Ref. [13]. To explain its improvements made in this work, we first present the necessary relations from [13]. Evolution of a binary alloy is described by a stochastic kinetic equation written in a finite-difference form for a short time interval δt:

$$\delta c_i \equiv c_i(t+\delta t) - c_i(t) = \delta c_i^d + \sum_{j_{nn}(i)} \delta n_{ij}^f, \qquad (4)$$

where c_i is the occupation of site i by the minority (copper) atoms averaged over some locally equilibrated vicinity of this site, and the "diffusional" term δc_i^d corresponds to the average atomic transfer for a certain effective direct atomic exchange (DAE) model:

$$\delta c_i^d\{c_k\} = \sum_{j_{nn}(i)} M_{ij} 2 \operatorname{sh} \frac{\beta(\lambda_j - \lambda_i)}{2} \delta t. \qquad (5)$$

Here, λ_i is the local chemical potential of site i given by Eq. (20) in [13], and M_{ij} is the generalized mobility:

$$M_{ij} = \gamma_{\alpha h}^{eff} b_{ij}^h \exp \frac{\beta(\lambda_i + \lambda_j)}{2}. \qquad (6)$$

The factor b_{ij}^h in (6) is some function of local concentrations c_i, given by Eq. (33) in [13], while $\gamma_{\alpha h}^{eff}$ is an effective rate of exchanges between neighboring minority and host atoms, α and h (copper and iron), which is proportional to the product of the analogous rates

$\gamma_{\alpha v}$ and γ_{hv} respectively describing exchanges between a vacancy and an atom α and between a vacancy and an atom h:

$$\gamma_{\alpha h}^{eff} = \gamma_{\alpha v}\gamma_{hv}\nu(t). \tag{7}$$

Here, the function $\nu(t)$ defined in Eq. (36) in [13] determines the "time rescaling" between the original vacancy-mediated exchange model and the effective DAE model used for simulations. The temporal evolution of this DAE model is described by the "reduced time" t_r having the meaning of the mean number of atomic exchanges $\alpha \leftrightharpoons h$ for the physical time t. The reduced time t_r is related to this time t by the following differential or integral relations:

$$dt_r = \gamma_{\alpha h}^{eff}\,dt, \quad \gamma_{\alpha h}^{eff} = \gamma_{\alpha v}\gamma_{hv}\nu(t),$$
$$t = \int_0^{t_r} \frac{dt'_r}{\gamma_{\alpha h}^{eff}(t'_r)}. \tag{8}$$

The form of the function $t(t_r)$ is discussed below. As mentioned in Ref. [18], Eqs. (4)–(8) can be derived not only for a simplified "quasi-equilibrium" model used in [13], which disregards renormalizations of the effective interactions in a nonequilibrium alloy (whose importance for the diffusion kinetics was noted in [19]), but also with these renormalizations taken into account.

The last term δn_{ij}^f in Eq. (4) is a fluctuative atomic transfer through the bond ij described by the Langevin-noise-type method: each δn_{ij}^f is treated as a random quantity with the Gaussian probability distribution

$$W(\delta n_{ij}^f) = A_{ij}\exp\left[(-\delta n_{ij}^f)^2/2D_{ij}\right], \tag{9}$$

where A_{ij} is the normalization constant. The dispersion D_{ij} is related to the mobility M_{ij} and the time interval δt in Eq. (5) by the "fluctuation–dissipation"-type relation

$$D_{ij} = \langle(\delta n_{ij}^f)^2\rangle = 2M_{ij}\,\delta t. \tag{10}$$

As discussed in detail in [13], for the nonequilibrium statistical systems under consideration, Langevin-noise-type equations (4)–(10) should be supplemented by a "noise filtration" procedure eliminating the short-wave contributions to fluctuations δn_{ij}^f, because these contributions are already included in the diffusional term δc_i^d obtained by statistical averaging over these short-wave fluctuations. Therefore, in the last term in Eq. (4), the full fluctuative transfer δn_{ij}^f should be replaced by its long-wave part δn_{ij}^{fc}. This can be done by introducing a proper cut-off factor $F_c(\mathbf{k})$ in the Fourier component $\delta n_{f\alpha}(\mathbf{k})$ of the full fluctuation $\delta n_{ij}^f \equiv \delta n_\alpha^f(\mathbf{R}_{s\alpha})$, where $\mathbf{R}_{s\alpha}$ denotes the position of the ij bond center in the appropriate crystal sublattice α formed by these centers [12]:

$$\delta n_{ij}^f \to \delta n^{fc}(\mathbf{R}_{s\alpha}) = \sum_{\mathbf{k}} \exp(-i\mathbf{k}\cdot\mathbf{R}_{s\alpha})\,\delta n^f(\mathbf{k})F_c(\mathbf{k}),$$
$$\delta n^f(\mathbf{k}) = \frac{1}{N}\sum_{\mathbf{R}_{s\alpha}} \exp(i\mathbf{k}\cdot\mathbf{R}_s)\,\delta n^f(\mathbf{R}_{s\alpha}), \tag{11}$$

where N is the total number of lattice sites (or atoms) in the crystal. The cut-off factor $F_c(\mathbf{k})$ for the BCC lattice can be taken in a Gaussian-like form:

$$F_c^{\mathrm{BCC}}(\mathbf{k}) = \exp\left[-4g^2(1-\cos\varphi_1\cos\varphi_2\cos\varphi_3)\right], \tag{12}$$

where $\varphi_\nu = k_\nu a/2$, k_ν is the vector $\mathbf{k}$ component along the main crystal axis ν, and a is the BCC lattice constant. At $g^2 \gg 1$, expression (12) reduces to the Gaussian $\exp(-k^2l^2/2)$ with $l = ga$. Therefore, the reduced length $g = l/a$ characterizes the mean size of locally equilibrated subsystems.

This size, generally, varies with the aging time t or t_r. In particular, after creation of a supercritical precipitate, the degree of local equilibrium in the adjacent region should increase compared with other regions where such precipitates are not yet born. Therefore, after the completion of nucleation at some reduced time t_{rN} (which can be estimated as the time for which the density of precipitates reaches its maximum), the alloy should rapidly approach a two-phase equilibrium, and the length $l = ga$ should become large, which should lead to a sharp decrease in the fluctuative terms $\delta n^f = \delta n^{fc}$ in Eqs. (11) and (4).

To describe this physical picture with the minimal number of model parameters, the time dependence $g(t_r)$ was approximated in [13] by a simple one-parameter expression (71) with a break at $t_r = t_{rN}$. Here, we use a smooth two-parametric expression for $g(t_r)$,

$$g(t_r) = g_0(1 + t_r^2/t_0^2), \tag{13}$$

where g_0 and t_0 have the respective order of magnitude of the reduced critical radius R_c/a and the reduced nucleation time t_{rN}.

To estimate the values g_0 and t_0 within the SSM, we can use the "maximum thermodynamic gain" principle discussed in detail in [13]: we suppose that the "most realistic" values of these parameters correspond to the

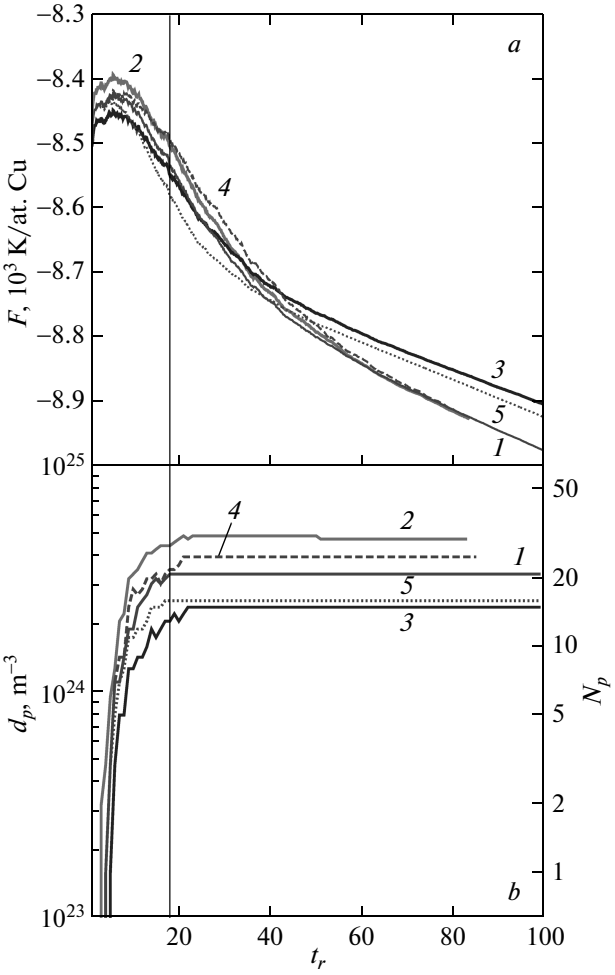

Fig. 2. *a*) Evolution of the free energy per copper atom, $F(t_r)$, and *b*) the density $d_p(t_r)$ of supercritical precipitates or their total number $N_p(t_r)$ within the simulation volume $V_s = (64a)^3$, obtained for the state A in the SSM simulations with different g_0 and t_0. Curves *1*, *2*, and *3* correspond to $t_0 = 40$ and $g_0 = 1.4$, 1.35, and 1.45, respectively. Curves *4* and *5* correspond to $g_0 = 1.4$ and $t_0 = 50$ and 30, respectively. Thin vertical line corresponds to $t_{rN} = 18$

minimum of the free energy of an alloy after the completion of nucleation. In Fig. 2, to illustrate this variational method for estimating g_0 and t_0, we present the SSM-simulated temporal dependences of the free energy per copper atom for the state A in Table 1 at several g_0 and t_0 close to their "optimal" values. The free energy $F = F(c_i)$ was calculated in accordance with Eq. (24) in [13] with the simulated $c_i = c_i(t_r)$ dependences. For simplicity, the initial state was taken uniform: $c_i(0) = c = \text{const}$, and hence the initial increase of F at $t_r \lesssim 0.3t_{rN}$ seen in Fig. 2*a* is related just

Table 2. The parameters g_0 and t_0 in (13), the reduced nucleation time t_{rN}, and the maximum precipitate density d_{max} (in 10^{24} m^{-3}) for the alloy states considered

Alloy state	g_0	t_0	t_{rN}	d_{max}^{SSM}	d_{max}^{KMC}
A	1.4	40	~ 20	3.4	4.0
B	1.4	30	~ 20	5.4, 5.8	6.1
C	1.45	20	~ 10	14.9	14.2
D	1.4	10	~ 10	9.7	10.1
E	1.6	10	~ 10	13.6	11.2
F	1.6	5	~ 5	9.9	8

to switching on the fluctuations at $t_r = 0$. Figure 2*a* shows that the influence of this spurious increase in F ceases only at $t_r \gtrsim 2t_{rN}$, while at too long times $t_r \gtrsim 4t_{rN}$, the fluctuations are effectively switched off according to Eqs. (11)–(13). Therefore, to estimate the parameters g_0 and t_0, we usually consider the interval $2t_{rN} \gtrsim t_r \gtrsim 4t_{rN}$. For most of the states considered, the free energy $F(t_r)$ has a distinct minimum with respect to g_0 and t_0 there, as is illustrated by Fig. 2*a*. Figure 2*b* illustrates the sensitivity of the precipitate density d_p to the choice of g_0 and t_0. The resulting scatter in simulated $d_p(t_r)$ usually lies within the statistical errors of simulations.

In Table 2, we present the values of g_0 and t_0 in (13) estimated as described above. For the state G, the simulations are time consuming, and therefore such estimates have not been made in this work. To assess the validity of our SSM simulations, in the two last columns of Table 2, we compare the values of the maximum density d_{max} of supercritical precipitates obtained in the SSM simulations with those obtained in the KMC simulations. For the state B in Table 2, two values d_{max}^{SSM} correspond to the two simulations (shown in Fig. 6 below) with different random number sets. We see that the SSM and the KMC results for d_{max} agree within the statistical errors of simulations.

The precipitation kinetics is usually characterized by the density and the mean radius of supercritical precipitates, $d_p(t)$ and $R(t)$, defined by the relations

$$d_p(t) = \sum_k \nu_k(t)/V_s,$$
$$R(t) = \sum_k \nu_k(t)R_k \Big/ \sum_k \nu_k(t). \qquad (14)$$

Here, $\nu_k(t)$ is the number of clusters containing k cop-

per atoms, V_s is the simulation volume, R_k is defined similarly to Eq. (3), $R_k = a(3k/8\pi)^{1/3}$, and the sums over k in (14) include only clusters with $k \geq N_c$, where N_c is the "critical" size chosen. As discussed in [9, 13] and below, the exact choice of this size (if reasonable) usually does not significantly affect the $d_p(t)$ and $R(t)$ values in (14). Therefore, we take N_c close to its "thermodynamic" value N_c^{th} in Table 1, setting $N_c = 15$, 15, 12, 11, 8, 5, and 28 copper atoms for the respective state A, B, C, D, E, F, and G. The temporal dependences $d_p(t_r)$ and $R(t_r)$ obtained in our SSM simulations with such N_c are illustrated in Fig. 3 for the state A; for the other states considered, these dependences are similar. Figure 3 illustrates the sequence of four well-defined stages of precipitation accepted in the classical theory of nucleation (see, e. g., [20]): incubation, nucleation, growth, and coarsening, as well as the presence of an "intermediate" stage between growth, and coarsening (seen also in the simulations in [20] and discussed in detail in [21]), which corresponds to the beginning of Ostwald ripening when the bigger precipitates already start to grow due to dissolving the smaller ones, but the latter do not disappear yet. For brevity, this intermediate stage is called "pre-coarsening" in what follows.

We now discuss the "time rescaling" function $t(t_r)$ in Eq. (8) determined by the temporal dependence of the effective direct exchange rate $\gamma_{\alpha h}^{eff} = \gamma_{\mathrm{CuFe}}^{eff}(t_r)$. For simplicity, this dependence was approximated in [13] by a simple two-parameter expression (77), which included sharp breaks at some t_r. Better interpolations for $t(t_r)$ can be obtained from the comparison of the SSM and the KMC results for the density and the mean size of precipitates, that is, from an approximate solution of two equations:

$$d_p^{KMC}(t) = d_p^{SSM}(t_r), \quad R_{KMC}(t) = R_{SSM}(t_r). \quad (15)$$

Our estimates of the functions $t(t_r)$ for which both equations (15) are satisfied with a reasonable accuracy showed that for all alloy states considered, these functions have a similar shape characterized by the presence of four intervals of t_r with an approximately constant value of the derivative $D = d\ln t/d\ln t_r \propto 1/\gamma_{\mathrm{CuFe}}^{eff}$ within each interval. These four intervals are determined by the inequalities

$$\begin{aligned} &(1)\ t_r < t_{r1}, \quad (2)\ t_{r1} < t_r < t_{r2}, \\ &(3)\ t_{r2} < t_r < t_{r3}, \quad (4)\ t_{r3} < t_r, \end{aligned} \quad (16)$$

where the respective point t_{r1}, t_{r2}, or t_{r3} approximately separates the stages of nucleation and growth, growth and pre-coarsening, or pre-coarsening and coarsening,

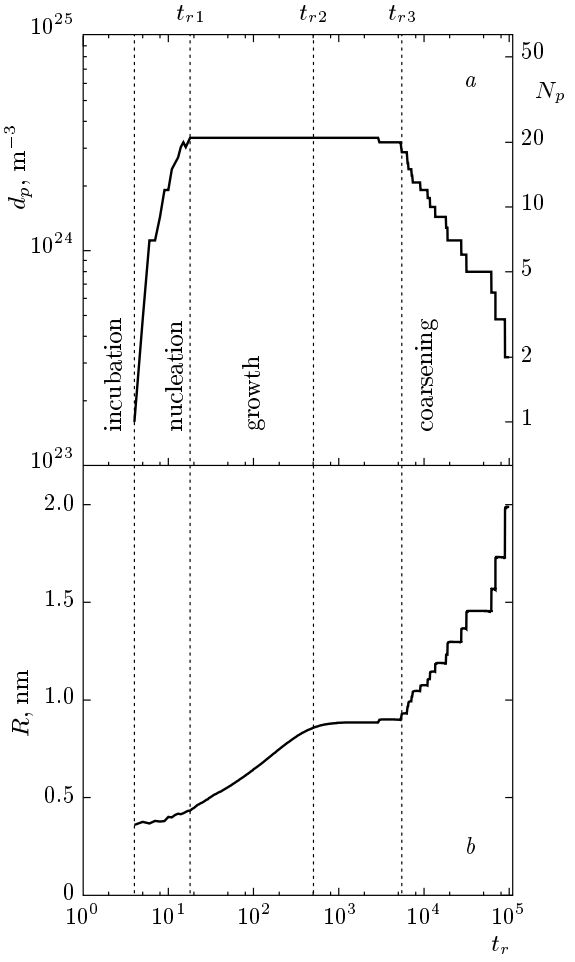

Fig. 3. *a*) Evolution of the density of precipitates, $d_p(t_r)$, and *b*) their mean radius $R(t_r)$ obtained in the SSM simulations for the state A in Table 1. Dotted vertical lines correspond to the values t_{ri} in Eqs. (16)

as is illustrated by Fig. 3. Therefore, within each interval (i), we use a simple power-law interpolation

$$t = A_i t_r^{D_i} \quad (17)$$

with the values of parameters t_{ri}, D_i, and A_i given in Table 3. For the state F with the relatively low temperature $T = 561$ K, our KMC simulations (illustrated in Fig. 11 below) are time consuming and reach only the growth stage, and hence interpolation (17) has not been constructed for this state.

The functions $t(t_r)$ obtained are shown in Fig. 4. To compare the precipitation parameters at different temperatures T for which the equilibrium vacancy concentration $c_v^{eq}(T)$ can be very different, in Fig. 4 we use the "scaled" time $t_s(t_r)$ defined as

$$t_s(t_r) = t(t_r)\, c_v^{eq}(T)/c_v^{eq}(773\,\mathrm{K}), \quad (18)$$

Table 3. Values of the parameters t_{ri}, D_i and A_i (in hours) in (16) and (17)

Alloy state	t_{r1}	t_{r2}	t_{r3}	D_1	D_2	D_3	D_4	A_1	A_2	A_3	A_4
A	18	506	5500	0.7	0.23	0.04	0.3	0.061	0.24	0.77	0.08
B	7.4	192	7240	1.1	0.33	0.11	0.4	0.021	0.097	0.30	0.023
C	2.9	70	3000	1.85	0.23	0.12	0.35	0.013	0.071	0.11	0.018
D	5	60	2300	1	0.23	0.08	0.27	0.027	0.14	0.26	0.026
E	3.2	60	2200	1.5	0.19	0.08	0.3	0.015	0.16	0.25	0.012

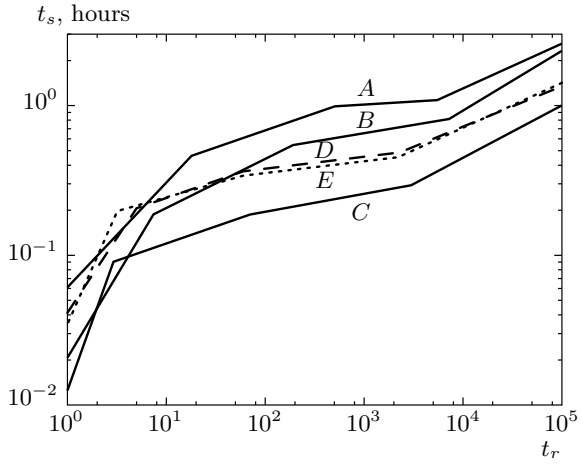

Fig. 4. The scaled physical time $t_s(t_r)$ defined by Eqs. (17) and (18) versus the reduced time t_r. Each curve corresponds to the alloy state indicated by a symbol near this curve

to cancel the standard scaling factor $1/c_v^{eq}$ in the t_s value. For the $c_v^{eq}(T)$, we use Soisson and Fu's estimate [9]

$$c_v^{eq}(T) = \exp\left(-\varepsilon_v^{for}/T\right), \quad \varepsilon_v^{for} = 2.18\,\text{eV}. \tag{19}$$

The SSM values $d_p^{SSM}(t)$ and $R_{SSM}(t)$ found using Eqs. (17) and Table 3 are compared with the appropriate KMC results in Figs. 5–10. We note that interpolation (17) includes some minor breaks at the points $t_r = t_{ri}$, which are seen in Fig. 4. These breaks can be removed by introducing some smooth matching of two lines (17) adjacent to each point t_{ri}, which also leads to a better agreement between the SSM and the KMC results in Figs. 5–10. But in this work, to avoid introducing too many interpolation parameters, we use the simpler interpolation (17), which seems to provide a sufficiently nice description of precipitation.

As discussed in Ref. [13], the significant changes of derivatives $D_i \sim 1/\left(\gamma_{\text{CuFe}}^{eff}\right)_i$ between different intervals i seen in Fig. 4 can be related to the strong vacancy trapping by copper precipitates and to the changes in the scale of this trapping in the course of precipitation. In particular, the relatively low values of the derivatives D_3 at the pre-coarsening stage can be related to the strong vacancy trapping for this stage (illustrated in Fig. 6*a* in [9]) which should result in a sharp increase in the effective rate $\gamma_{\text{CuFe}}^{eff}$ in Eq. (8) [13]. We also note the similarity of the curves $t_s(t_r)$ for different alloy states in Fig. 4, as well as rather smooth variations of the parameters D_i and A_i in Table 3 under changes of the concentration x and temperature T corresponding to these different states. This seems to reflect a great similarity of the vacancy trapping effects within each interval i for the different alloy states. This similarity can be used for various SSM-based extrapolations of KMC simulations, in particular, for SSM-based simulations of precipitation in Fe–Cu alloys at most different concentrations x and temperatures T with the use for the parameters t_{ri}, D_i and A_i in (16) and (17) of some interpolations between their values presented in Table 3. This similarity is also used for extrapolations of the KMC simulations to the first stages of coarsening discussed below.

To conclude this section, we note that the simplified treatment of fluctuations based on Eqs. (9)–(13) can properly describe nucleation and growth only when these two processes are sufficiently separated from each other, such that switching off fluctuations after the completion of nucleation, as is implied by Eq. (13), can be justified. Figures 5–10 show that this condition is more or less satisfied for the first five states in Table 1. At the same time, for states F and G, that is, at low temperatures $T \lesssim 300$°C or at low supersaturations $s \lesssim 0.2$, the nucleation, growth, and pre-coarsening stages overlap very strongly, as Figs. 11, 12 and 17 show, and the simple model in Eqs. (9)–(13) implying the type of evolution shown in Fig. 3 can hardly be applicable. Therefore, for states F and G, only KMC simulations are presented in this paper. Further re-

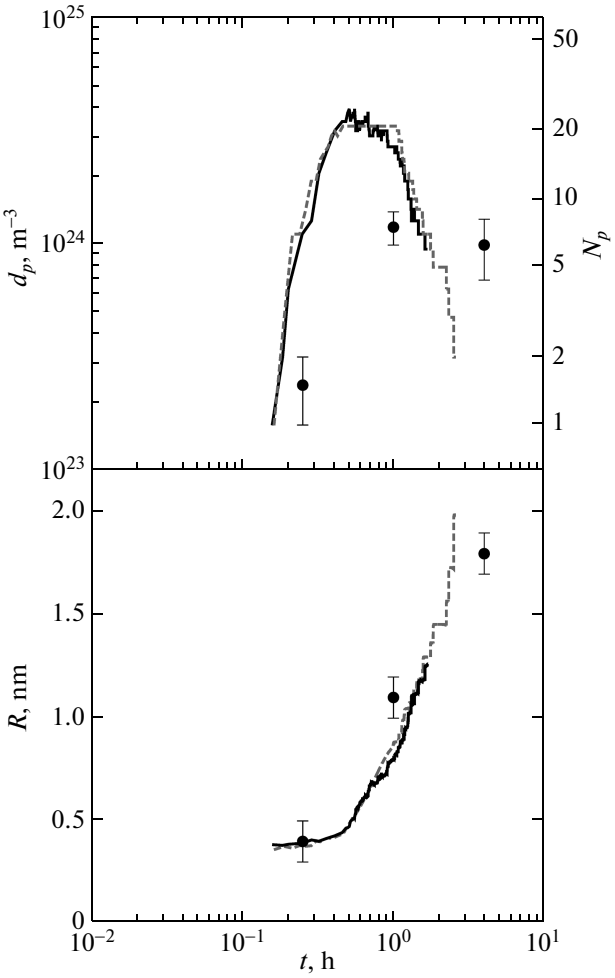

Fig. 5. Evolution of the density of precipitates $d_p(t)$ (top figure), and their mean radius $R(t)$ (bottom figure) obtained in our simulations for the state A with $x = 1.17$ (in at. %, here and below), $T = 773$ K for the critical size of $N_c = 15$ copper atoms. The right scale shows the number of precipitates within the simulation volume $V_s = (64a)^3$. Solid curves correspond to the KMCM and dashed curves to the SSM. Points show experimental data in [6] for the multicomponent steel NUCu-140 with the same $x_{\mathrm{Cu}} = 1.17$ and $T = 773$ K for $N_c = 11$

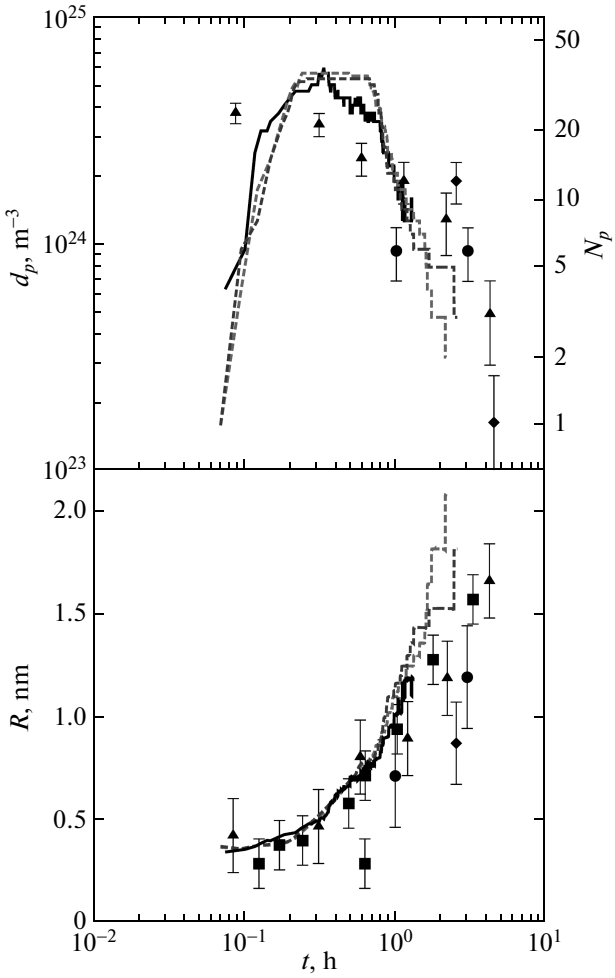

Fig. 6. The same as in Fig. 5 but for the state B with $x = 1.34$ and $T = 773$ K for $N_c = 15$. Two dashed curves correspond to the two SSM simulations with different random number sets. Symbols correspond to experimental data for state B: circles, [1]; triangles, [2]; and rhombi, [3]

finements of the SSM are evidently needed to use this method at the low temperatures or low supersaturations mentioned.

4. RESULTS OF SIMULATIONS AND COMPARISON WITH EXPERIMENTS

The results of our simulations together with the available experimental data for some Fe–Cu and Fe–Cu-based alloys are presented in Figs. 5–17. Figures 5–12 show the temporal evolution of the density and the mean radius of precipitates, $d_p(t)$ and $R(t)$. We note that for the state F in Fig. 11, this evolution is described in terms of the scaled time t_s defined by Eq. (18) (with the replacement $t_r \to t$), because the equilibrium vacancy concentration $c_v^{eq}(T)$ at the low temperature $T = 561$ K considered there is negligibly small, while actually (in particular, in the experiments in [4]), the precipitation at such a low T occurs only in irradiated materials where the vacancies (together with the interstitial atoms) are formed due to irradiation.

Figures 13–16 illustrate the concentration and temperature dependences of the maximum precipitate den-

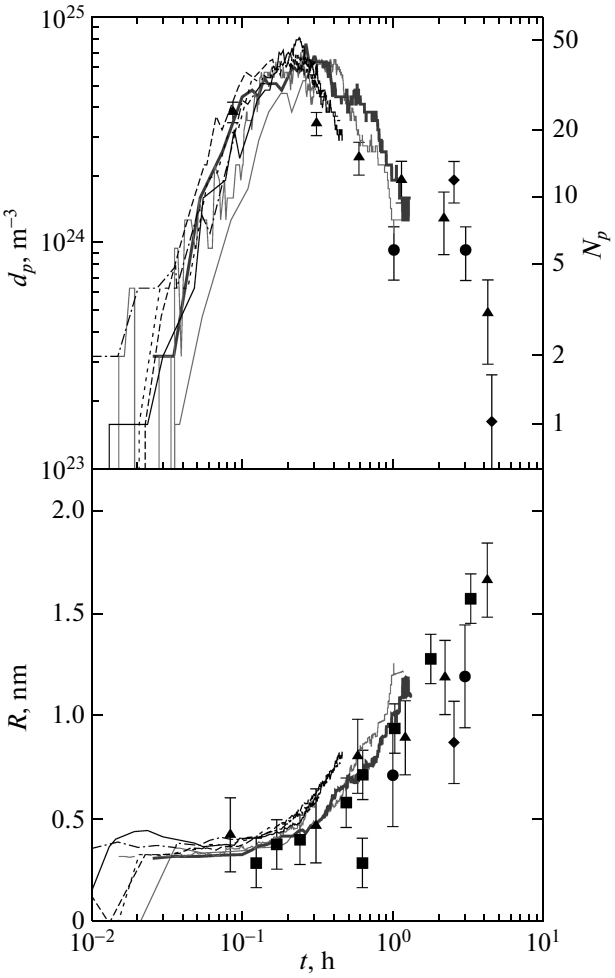

Fig. 7. The same as in Fig. 6 but for seven different KMC simulations for $N_c = 10$. The thick solid line corresponds to the same KMC simulation as that shown in Fig. 6 by the thick line for $N_c = 15$

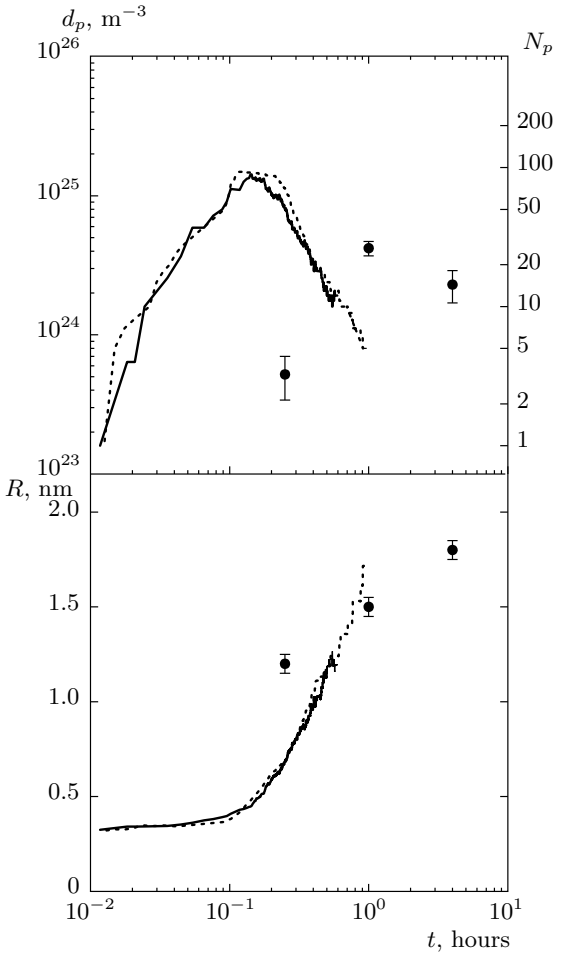

Fig. 8. The same as in Fig. 5 but for the state C with $x = 1.82$ and $T = 773$ K for $N_c = 12$. Points show the experimental data in [5, 6] for the multicomponent steel NUCu-170 with the same $x_{\mathrm{Cu}} = 1.82$ and $T = 773$ K for $N_c = 11$

sity $d_p^{max} = d_{max}$ and of some temporal characteristics of precipitation, t^{max}, t^c and $t^{c,0.1}$, defined by the relations

$$d_p(t^{max}) = d_{max}, \tag{20}$$

$$t^c = t(t_{r3}), \tag{21}$$

$$d_p(t^{c,0.1}) = 0.1 d_{max}, \tag{22}$$

where the reduced time t_{r3} and the function $t(t_r)$ in (21) are the same as in (16) and (17). The time t^{max} usually corresponds to the completion of nucleation or the beginning of growth; the time t^c approximately corresponds to the onset of coarsening, and $t^{c,0.1}$ can characterize the time of completion of the first stage of coarsening and the beginning of its more advanced stages. In what follows, for brevity, t^{max} is called the "nucleation time" and $t^{c,0.1}$, the "advanced coarsening time". In Figs. 13–16, we also present the experimental estimates of t^{max} and $t^{c,0.1}$, but not of t^c, because such estimates are usually not reliable for the onset of coarsening.

Figure 17 illustrates temporal evolution of the precipitate size distributions observed in our simulations. In the caption to this figure, we use the times $t^{N,\alpha}$ and $t^{c,\alpha}$ defined similarly to the "nucleation time" t^{max} and the "advanced coarsening time" $t^{c,0.1}$ in Eqs. (20) and (22):

$$d_p(t^{N,\alpha}) = \alpha d_{max}, \quad t^{N,\alpha} < t^{max}, \tag{23}$$

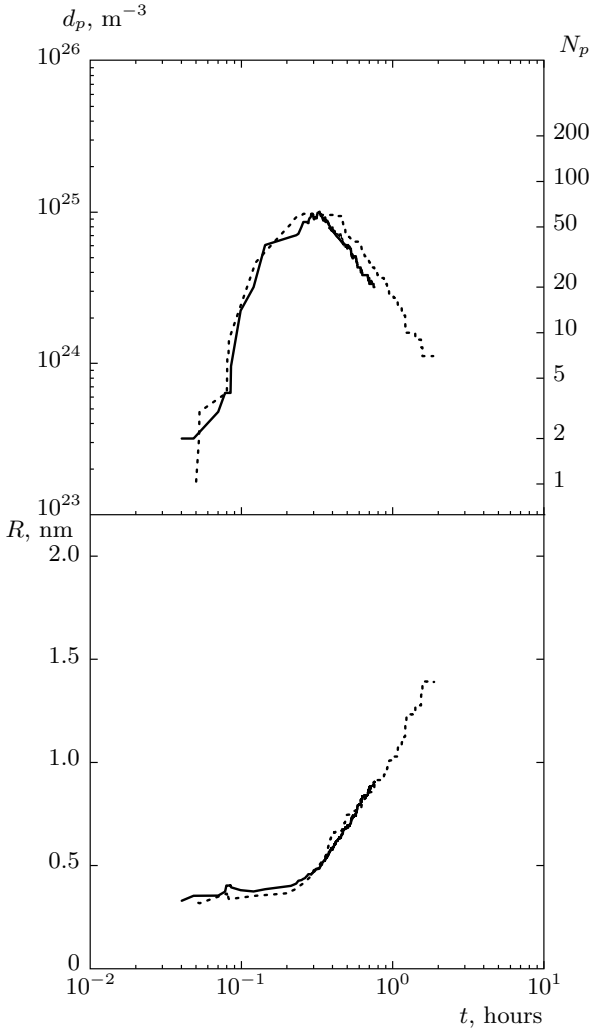

Fig. 9. The same as in Fig. 5 but for the state D with $x = 1.34$ and $T = 713$ K for $N_c = 11$

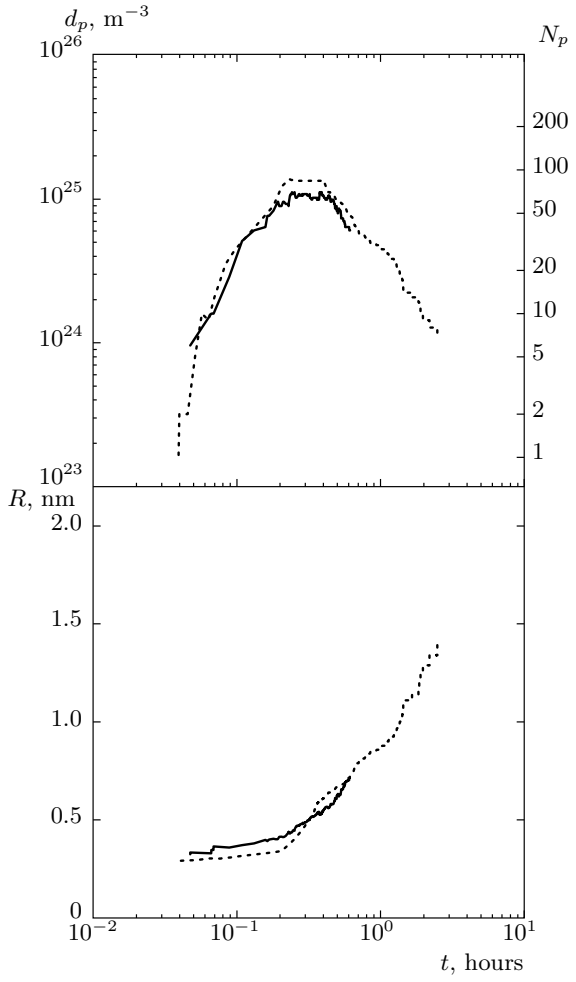

Fig. 10. The same as in Fig. 5 but for the state E with $x = 1.34$ and $T = 663$ K for $N_c = 8$

$$d_p(t^{c,\alpha}) = \alpha d_{max}, \quad t^{c,\alpha} > t^{max}, \tag{24}$$

where the number α is less than unity. The times $t^{N,\alpha}$ qualitatively correspond to the nucleation stage and $t^{c,\alpha}$, to the coarsening stage.

We discuss the results presented in Figs. 5–17. First, Figs. 5–12 and 17 show that the above-mentioned strong attraction between a vacancy and a copper atom leads to a great difference in the precipitation kinetics between iron–copper alloys and alloys with no such attraction, such as the alloys described by simplified models with the time-independent effective direct exchange rates $\gamma_{\alpha h}^{eff}$ in (8), for which this kinetics is illustrated in Fig. 3, or the models with a relatively weak vacancy–minority-atom interaction for which this kinetics is illustrated by Fig. 1 in [20] or Fig. 4 in [21]. For such simplified models, the presence of five well-defined stages of evolution shown in Fig. 3 is characteristic, including the distinct pre-coarsening stage mentioned above. On the contrary, in Figs. 5–12, such an intermediate pre-coarsening stage is not seen, the "pure nucleation" and "pure growth" stages are relatively short (if exist at all), and the nucleation, growth, and pre-coarsening stages significantly overlap with each other. This is also illustrated by the size distribution functions $\nu_k(t)$ in Fig. 17, which seem to imply that the nucleation, growth and pre-coarsening processes at $0.5t^{max} \lesssim t \lesssim t^{max}$ occur simultaneously. As discussed in [13], these kinetic features seem to be mainly related to the strong vacancy trapping by copper precipitates, which leads to a large acceleration of both the growth and the Ostwald ripening processes compared with the alloys with no such trapping.

Figures 5–10 also show that for the first five alloy states in Table 1, the simplified direct-atomic-exchange

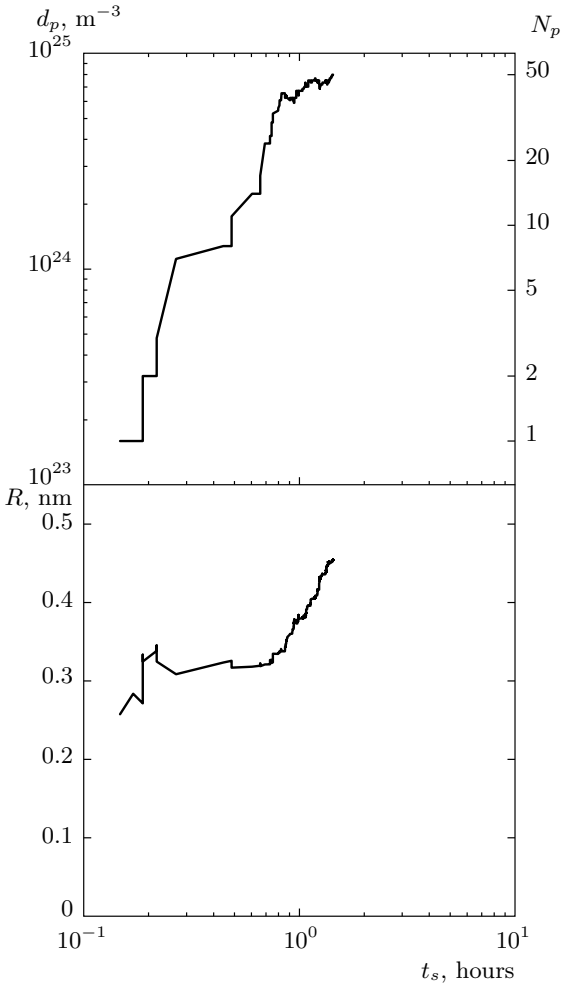

Fig. 11. The same as in Fig. 5 but for the state F $x = 0.78$, $T = 561$ K for $N_c = 5$

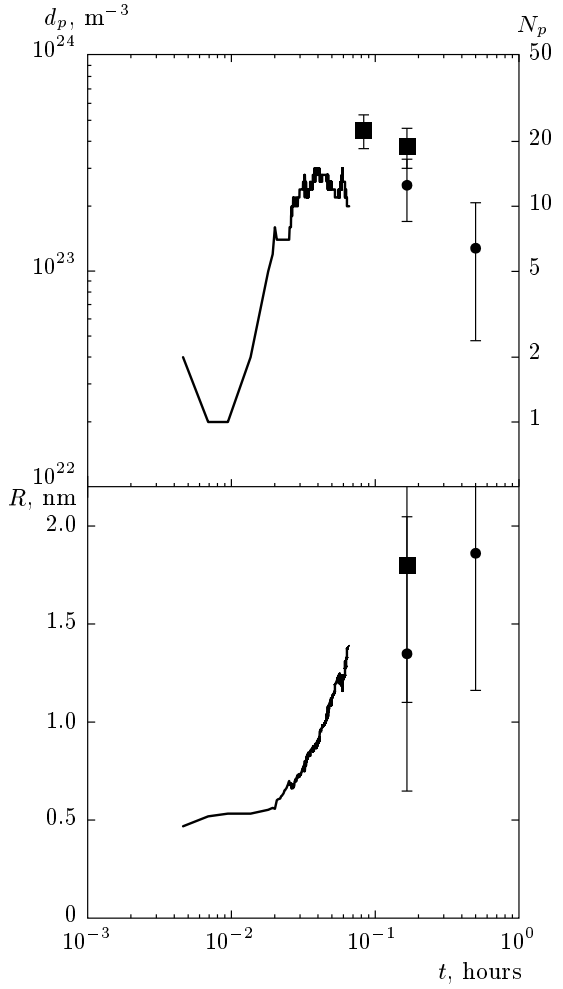

Fig. 12. The same as in Fig. 5 but for the state G with $x = 1.15$, $T = 873$ K for $N_c = 28$. Solid symbols show experimental data in [7] for the following alloys aged at $T = 873$ K: circles, binary Fe–1.15Cu; squares, ternary Fe–1.14Cu–0.99Mn. The right scale shows the number of precipitates, N_p, within simulation volume $V_s = (128a)^3$

model in Eqs. (4)–(12), using the above-mentioned maximum thermodynamic gain principle and the simple interpolation (17), describes the precipitation kinetics in good agreement with the KMCM. Discrepancies between the SSM and the KMCM results are usually within statistical errors of simulations, and these discrepancies can be reduced even stronger if the smoothed interpolations mentioned above are used instead of simpler expressions (17).

Figures 5, 6, and 8–10 also illustrate the opportunities to use the SSM to extrapolate the KMC simulations to longer evolution times. As mentioned, the KMC simulations of coarsening are time consuming, unlike the SSM simulations. At the same time, the above-described considerations about the physical nature of the "time rescaling" function $t(t_r)$ in (17) allow expecting that this function preserves its shape for the first stages of coarsening at least up to $t \sim t^{c,0.1}$, until the later, more advanced stages of coarsening (including the asymptotic Lifshits–Slyozov–Wagner stage [22, 23]) start. Therefore, we can use the SSM simulated $d_p(t_r)$ and $R(t_r)$ and Eq. (17) to estimate the $d_p(t)$ and $R(t)$ values for those t for which the KMC results are not available. This is shown in Figs. 5, 6, and 8–10.

Figures 6 and 7 also illustrate some methodical points. Two dashed curves in Fig. 6 correspond to two SSM simulations with different random number sets, and hence their difference illustrates the statistical scatter of the SSM simulation results. We see that this scatter is significant only at the very end of simulations

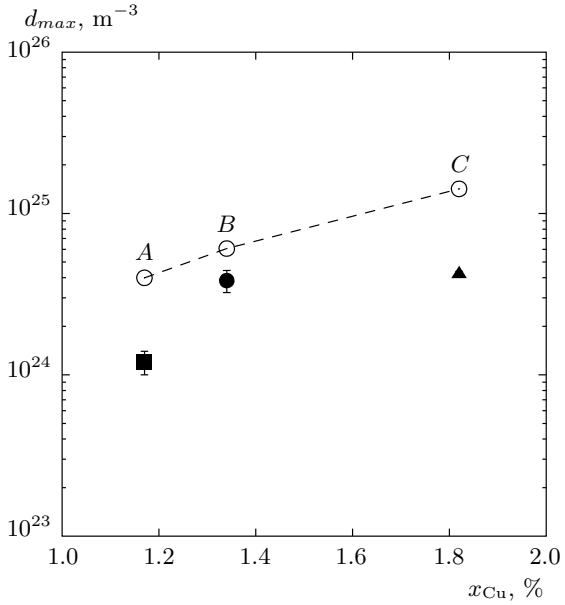

Fig. 13. Concentration dependence of the maximum density of precipitates d_{max} for decomposition of Fe–xCu and Fe–Cu-based alloys at $T = 773$ K. Open symbols here and below correspond to our simulations and solid symbols, to experiments. The solid circle corresponds to the experiments in [2] for state B, while solid square and solid triangle, to the respective experiments in [5, 6] for the multicomponent steel NUCu-140 with $x_{\mathrm{Cu}} = 1.17$ and NUCu-170 with $x_{\mathrm{Cu}} = 1.82$. Dashed lines here and below are drawn to guide the eye

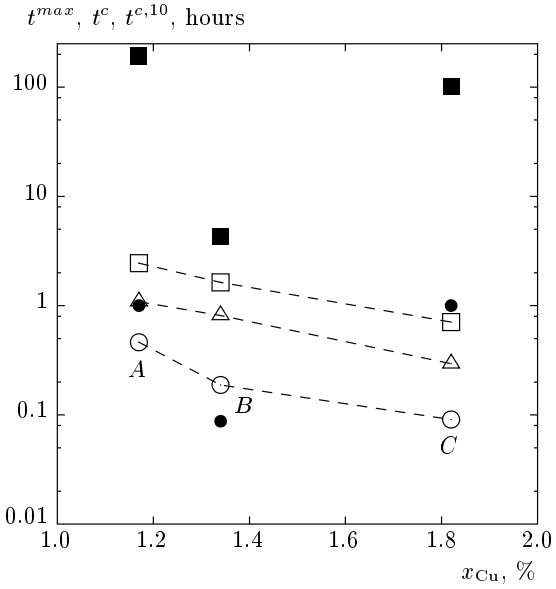

Fig. 14. Concentration dependence of temporal characteristics of precipitation: t^{max} (circles), t^c (triangles), and $t^{c,10}$ (squares), defined by Eqs. (20), (21), and (22), at $T = 773$ K. The solid circle and the solid square at $x_{\mathrm{Cu}} = 1.17$ or $x_{\mathrm{Cu}} = 1.82$ respectively correspond to the data in [5, 6] for the steel NUCu-140 or NUCu-170, while the solid circle and solid square at $x = 1.34$ correspond to the data in [1–3] for state B

when the total precipitate number N_p becomes small. Similarly, seven different KMC simulations shown in Fig. 7 illustrate the statistical scatter of the KMC simulation results. The effect of the choice of the "critical" size N_c in Eqs. (14) on the simulated $d_p(t)$ and $R(t)$ values is illustrated in Figs. 6 and 7, which correspond to the same alloy state B but to the different N_c, 15 and 11 copper atoms, while the thick solid curve in both Fig. 6 and Fig. 7 corresponds to the same KMC simulation. We see that the variations of N_c produce noticeable effects on the simulated $d_p(t)$ and $R(t)$ only at the first stages of nucleation; later on, such effects become insignificant.

We discuss the concentration and temperature dependences of the kinetic characteristics of precipitation presented in Figs. 13–16. For the maximum precipitate density d_{max}, these dependences shown in Figs. 13 and 15 are mainly determined by the reduced supersaturation s (defined in Eq. (2) and Table 1), which characterizes the scale of the thermodynamic driving force for precipitation. For a given temperature T or a given concentration x, the d_{max} value increases with s, and at low $s \lesssim 0.3$ or high $T \gtrsim 800$ K, this increase is rather sharp. At the same time, Fig. 15 shows that at not low $s \gtrsim 0.3$–0.4 and not high T, the d_{max} value changes with T more slowly, and at $T \lesssim 700$ K, a further decrease in temperature makes little effect on d_{max}. This may imply that the slowing down of kinetics due to the strong vacancy–copper-atom correlations discussed below becomes important for these T. The temporal characteristics of precipitation shown in Figs. 14 and 16*b* decrease with increasing the supersaturation s, which can be explained by an increase in the thermodynamic driving force. At the same time, Fig. 16*a* shows that at not low $s \gtrsim 0.3 - 0.4$ and not high $T \lesssim 750$ K, the scaled times t_s^{max}, t_s^c and $t_s^{c,10}$ vary with temperature rather weakly. This can be explained by an interplay between an increase, with decreasing T, of both thermodynamic driving forces, which promote the evolution, and the vacancy–copper-atom correlations, which reduce the copper diffusivity D_{Cu} [9] and thereby slow down the evolution.

The temporal evolution of the precipitate size distributions $\nu_k(t)$ for alloy states B, F, and G is illustrated in Fig. 17. For states A and D, this evolution is

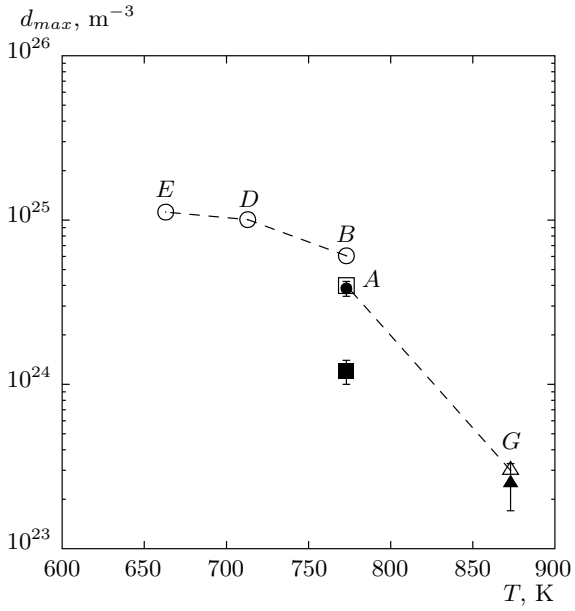

Fig. 15. Temperature dependence of the maximum density of precipitates in the course of decomposition of Fe–xCu and Fe–Cu-based alloys. Open circles correspond to states B, D and E with $x = 1.34$; open square, to state A with $x = 1.17$; and open triangle, to state G with $x = 1.15$. The solid circle corresponds to experiments in [2] for state B with $x = 1.34$; the solid square, to experiments in [6] for the steel NUCu-140 with $x_{\mathrm{Cu}} = 1.17$; and solid triangle, to experiments in [7] for state G with $x = 1.15$

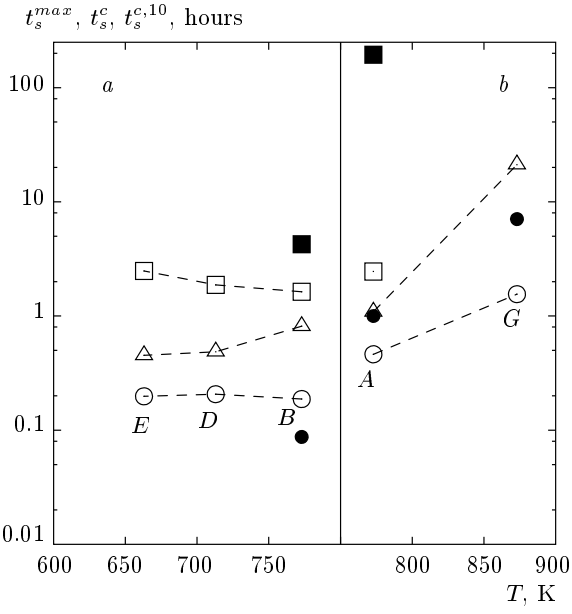

Fig. 16. Temperature dependence of the same temporal characteristics of precipitation as those in Fig. 14, but in terms of the scaled time t_s defined by Eq. (18): t_s^{max} (circles), t_s^c (triangles), and $t_s^{c,10}$ (squares). In figure a, the states B, D and E have the same $x = 1.34$, while solid circle and solid square correspond to experiments [2] for the state B with $x = 1.34$. In figure b, the state A corresponds to $x = 1.17$; solid circle and solid square at $T = 773$ K correspond to the data [6] for the steel NUCu-140 with $x_{\mathrm{Cu}} = 1.17$; and solid circle at $T = 873$ K corresponds to experiments [7] for the state G with $x = 1.15$

mainly similar to that for state B. First, we see that these distributions are usually rather broad, and the sizes of different precipitates are typically very different. Therefore, characterization of these sizes by only their mean value $R(t)$ used in Figs. 5–12 is oversimplified and incomplete. This is true not only for the coarsening stage (for which a great difference in the precipitate sizes is natural because the bigger precipitates coarsen due to the dissolution of smaller ones) but also for all other stages of precipitation. This can be related to the strong overlapping of the nucleation, growth, and pre-coarsening stages mentioned above.

The comparison of the distributions $\nu_k(t)$ at $t = t^{max}$ and $t = 1.1t^{max}$ (that is, of frames B2 and B3 or G2 and G3 in Fig. 17) also illustrates the significant overlapping of the growth and early coarsening stages. We see that the large majority of precipitates at $t = 1.1t^{max}$ continue to grow due to the absorption of copper atoms from the matrix, even though some smallest precipitates already start to dissolve. Such a significant overlap of the growth and early coarsening stages agrees with the observations in [3] for the Fe–1.34Cu alloys (state B in Table 1), and it was also noted in [6] for the NUCu steels.

Second, the comparison of the size distributions $\nu_k(t)$ at $t = t^{max}$ and $t = 1.1t^{max}$ also illustrates very sharp variations of these distributions with the evolution time t, in particular, at t corresponding to the beginning of coarsening, which is not clearly seen in the "averaged" description in Figs. 5–12. Third, Fig. 17 shows that the precipitate size distribution $\nu_k(t)$ for state G with the highest temperature $T = 873$ K is, generally, much more uniform than $\nu_k(t)$ for state D with the lower $T = 773$ K and 713 K, particularly for the early coarsening stage, which is illustrated by frames B4 and G4. In particular, in frames B4 and D4, we observe only one very big cluster with $k \sim 600$ copper atoms, numerous small clusters with $k < 200$ copper atoms, and 3 to 4 "middle-size" clusters with $k \sim 200$–300 atoms (the same features are also observed in $\nu_k(t)$ for states A and D not shown in Fig. 17), in

sharp contrast with frame G4 (as well as G2 and G3), where the cluster size distribution is rather uniform. This difference can be related to the weakening of the vacancy–copper-atom correlations at high T, which can enhance the copper diffusivity D_{Cu} and thereby promote the growth of many big precipitates for state G in contrast to state A, B, and D, but these points need further studies. Finally, the lower row in Fig. 17 illustrates features of precipitation at low temperatures $T \sim 300\,^{\circ}\mathrm{C}$ when vacancies (necessary for the atomic diffusion) are provided by irradiation. Figures F1–F3 illustrate a very strong overlapping of the nucleation growth and pre-coarsening stages, while the coarsening stage was not reached in these simulations.

We next compare the simulation results with the available experimental data. For state B and the KMC simulations shown in Figs. 6 and 7 by thick lines, the detailed comparison with various experiments was given in [9], with the conclusion that the predictions of simulations are reliable. The results presented in Figs. 6, 7, 14, and 16 can complement the discussion in [9] by two points. First, Figs. 6 and 7 confirm that the disagreements between simulations and experimental observations seem usually to lie within the statistical errors of simulations and the scatter of experimental results. Second, Figs. 6, 14, and 16 show that the SSM-based extrapolations of KMC simulations for the first stages of coarsening seem to agree with observations as well.

For the state G with $x = 1.15$ and $T = 873$ K, our simulations are compared with the data in [7] in Fig. 12. Because the supersaturation s and the precipitate density d_p for this state are rather low, these simulations are time consuming and include only the nucleation and growth stages, while the data in [7] seem to correspond to longer aging times and have significant errors. Within those errors, the simulation and experimental results in Fig. 12 can be considered as agreeing with each other, particularly for the maximum precipitate density d_{max}, although the simulated evolution times can be somewhat shorter than the observed ones. Solid squares in Fig. 12 correspond to a ternary Fe–Cu–Mn alloy and illustrate the effect of the third alloying element Mn on the precipitation kinetics. The presence of Mn seems to lead to an approximately two-fold increase in the maximum precipitate density d_{max} with respect to the analogous Fe–Cu binary, in a qualitative contrast to the effect of alloying elements on the d_{max} value in the NUCu steels discussed below.

In Figs. 5, 8, and 13–16, we compare the simulation results for state A or C with $T = 773$ K and $x = 1.17$ or 1.82 to the data in [5, 6] for the multi-component steels NUCu-140 and NUCu-170 with the same T and x_{Cu}. In addition to copper, these steels contain a number of alloying elements: C, Al, Ni, Si, Mn, Nb, P and S, 5.49 % on the total in NUCu-140, and 5.83 % in NUCu-170, while the partial concentrations of each alloying element in these two steels are very close to each other [5, 6]. Therefore, the differences in the precipitation kinetics for these two steels can be mainly related to the difference in the copper content x_{Cu}. Then the comparison of these kinetics for each of these steels to that for the analogous binary Fe–xCu alloy can elucidate the effect of alloying elements on the precipitation at different x_{Cu}. Qualitatively, these problems were discussed in [6]. Our simulations enable us to consider these points quantitatively. We also note that the critical sizes N_c for these two steels estimated in [5, 6], $N_c \approx 11$ copper atoms, are rather close to the estimates for their binary analogues presented in Table 1: $N_c^{th}(A) \approx 15$ and $N_c^{th}(C) \approx 12$ copper atoms.

We first discuss the nucleation and growth stages illustrated by Figs. 5 and 8. For the NUCu-140 or NUCu-170 steel, this respectively corresponds to $t \lesssim \lesssim 1$ h and $t \lesssim 0.25$ h, and the maximum precipitate density d_{max} in each steel is lower than in its binary analogue by about three times. However, for NUCu-140, both the values and the temporal dependences of $d_p(t)$ and $R(t)$ in Fig. 5 seem to not greatly differ from those simulated for the Fe–1.17Cu alloy, particularly for the nucleation stage, and the nucleation time t^{max} can also be similar. On the contrary, for NUCu-170, the data at $t = 0.25$ h shown in Fig. 8, particularly for the $R(t)$ value, sharply disagree with those simulated for the Fe–1.82Cu alloy, while the nucleation time t^{max} exceeds that for the Fe–1.82Cu alloy by an order of magnitude.

Therefore, our comparison seems to imply that the effect of almost the same content of alloying elements on the nucleation kinetics in NUCu-170 with the higher copper content $x_{\mathrm{Cu}} = 1.82$ is much stronger and qualitatively different from that in NUCu-140 with the lower $x_{\mathrm{Cu}} = 1.17$. Physically, this conclusion does not seem to be natural. In this connection, we note that this conclusion is mainly based on the data for the mean precipitate size in NUCu-170 at $t = 0.25$ h reported in [5], $R \approx 1.2$ nm. This value greatly exceeds the critical radius $R_c \approx 0.3$ nm estimated for this steel in [5], $R \approx 4R_c$. This should imply that in the course of the nucleation stage (supposed in [5] for the NUCu-170 at $t = 0.25$ h to explain a steep increase in the precipitate density $d_p(t)$ between $t = 0.25$ h and $t = 1$ h, seen in Fig. 8), the new-born precipitates grow extremely fast. Such a very sharp growth at the early nucleation stage

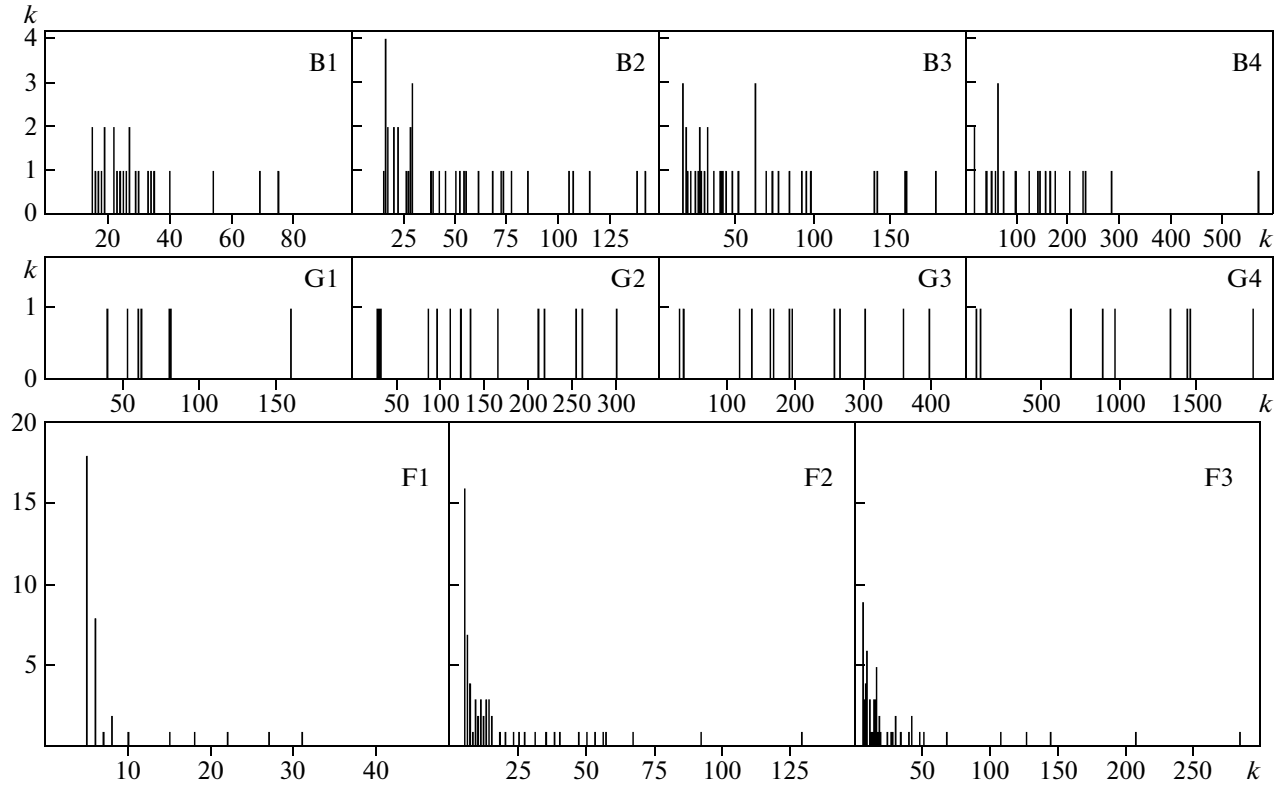

Fig. 17. Numbers of clusters containing k copper atoms, $\nu_k(t)$, observed in our KMC simulations. The first, second, and third and fourth row corresponds to the state B, G, and F in Table 1, respectively. Frame B1, B2, B3, or B4 corresponds to the time t equal to $t^{N,0.61}$, t^{max}, $1.1\,t^{max} = t^{c,0.94}$, or $t^{c,0.61}$; and frame G1, G2, G3, or G4, to $t^{N,0.47}$, t^{max}, $1.1t^{max} = t^{c,0.87}$, or $t^{c,0.67}$, respectively, where the time $t^{N,\alpha}$, t^{max} or $t^{c,\alpha}$ is defined by Eq. (23), (20), or (24). Frame F1, F2, or F3 corresponds to the scaled time t_s equal to $t_s^{N,0.48}$, $t_s^{N,0.94}$, or t_s^{max}, where the time $t_s^{N,\alpha}$ is defined by Eq. (23) with replacing $t \to t_s$, while $t_s^{max} = 1.45$ h corresponds to the end of our simulations for the state F

seems to be very unusual and, to our knowledge, was never observed in either experiments or simulations, as illustrated by Figs. 5–12. Therefore, the data about $R(t)$ in NUCu-170 at $t = 0.25$ h reported in [5] should possibly be taken with some caution.

For the coarsening stage, the results presented in Figs. 5, 8, and 14 fully agree with the main conclusions in [6] about a very strong slowing down of coarsening in the NUCu steels compared with Fe–Cu binaries. In particular, the advanced coarsening time $t^{c,0.1}$ for each of these steels exceeds that for its binary analogue by about two orders of magnitude. At the same time, the dependences of this advanced coarsening time $t^{c,0.1}$ on the copper content x_{Cu} for the NUCu steels and for their binary analogues shown in Fig. 14 seem to be similar.

The strong slowing down of coarsening in a ternary Fe–Cu–Mn alloy compared with its binary analogue Fe–Cu was also observed under neutron irradiation in [4]. On the contrary, the effects of alloying elements on the nucleation and growth kinetics in Fe–Cu–Mn alloys and in NUCu steels seem to differ qualitatively: according to Figs. 12 and 13, the d_{max} value for an Fe–Cu–Mn alloy is about twice higher, while for each of the NUCu steels, it is about three times lower than in its binary analogue. Therefore, for the coarsening stage, the effects of alloying elements on the decomposition kinetics in the multicomponent Fe–Cu-based alloys seem to be much more universal than those for the earlier stages of precipitation.

Such a universal slowing down of coarsening in the multicomponent Fe–Cu-based alloys with respect to their binary analogues Fe–Cu can be related to a significant segregation of alloying elements on the surface of precipitates [4–6], which can reduce the surface energy and thereby the thermodynamic driving force for coarsening. It can also be related to a weakening of the vacancy trapping at surfaces of precipitates due to this segregation. However, quantitative estimates of these effects seem to be absent yet.

5. CONCLUSIONS

We summarize the main results in this paper. The previously developed *ab initio* model and both the kinetic Monte Carlo (KMC) and the stochastic statistical methods are used to simulate the precipitation kinetics for seven binary Fe–Cu alloys with different copper concentrations x and temperatures T. Comparison of the results obtained with the available experimental data and other simulations enable us to make a number of conclusions about kinetic features of precipitation in both the binary Fe–Cu and the multicomponent Fe–Cu-based alloys.

First, we find that due to the strong vacancy trapping by copper precipitates, the precipitation kinetics in iron–copper alloys for all x and T considered differs notably from that observed for alloys with no such trapping: the "pure nucleation" and "pure growth" stages are relatively short, the nucleation, growth, and coarsening stages significantly overlap, while the intermediate "pre-coarsening" stage observed in some simulations for simplified alloy models (illustrated in our Fig. 3 and in Fig. 1 in Ref. [20]) is absent. In this connection, the presence of this pre-coarsening stage in simulations of precipitation in irradiated Fe–Cu alloys made in [21] can be related just to some oversimplifications of their model.

The concentration and temperature dependences of the maximum precipitate density d_{max}, the nucleation time t^{max}, and the advanced coarsening time $t^{c,0.1}$ defined by Eqs. (20) and (22) are illustrated in Figs. 13–16. At low supersaturations s, these dependences are rather sharp and seem to be mainly determined by the variations of the supersaturation $s(x,T)$ with x or T. At higher $s \gtrsim 0.3$, these temperature dependences become smoother and seem to be determined by an interplay between an enhancement, with lowering T, of both the thermodynamic driving forces promoting the evolution and the vacancy–copper-atom correlations reducing the copper diffusivity D_{Cu} and thereby slowing down the evolution.

Temporal evolution of the precipitate size distributions $\nu_k(t)$ is illustrated in Fig. 17. These distributions are typically rather broad, and they strongly vary with the evolution time t. Therefore, the conventional description of these sizes in terms of the mean precipitate size $R(t)$ is oversimplified and incomplete. We also find that for the alloy state G with the relatively high temperature $T = 873$ K, the precipitate size distribution $\nu_k(t)$ is more uniform than those observed for states A, B, and D with the lower temperatures $T = 773$ K and $T = 713$ K, particularly for the coarsening stage.

We also describe an improved version of the previously suggested stochastic statistical method for simulations of precipitation and show that this version can be used for various extrapolations of KMC simulations, in particular, for their extensions to the first stages of coarsening, for which the KMC simulations are time consuming.

The comparison of our simulated temporal dependences for the density and the mean size of precipitates in binary Fe–xCu alloys at $x = 1.34$ and $T = 773$ K and at $x = 1.15$ and $T = 873$ K to the available experimental data [1–3, 7] shows a reasonable agreement within both statistical errors of the simulations and the scatter of experimental results. The sizes N_c of critical precipitates calculated by the statistical method of Dobretsov and Vaks [14] and presented in Table 1 are close to those estimated in our KMC simulations and in the experiments in [5, 6] for NUCu steels.

The comparison of our simulation results for the Fe–1.17Cu and Fe–1.82Cu alloys to the data in [5, 6] about precipitation in NUCu-140 and NUCu-170 steels, which have the same copper content $x_{\mathrm{Cu}} = 1.17$ and $x_{\mathrm{Cu}} = 1.82$ and contain similar amounts of other alloying elements, enables us to assess the effects of these alloying elements on the precipitation kinetics. The maximum precipitate density d_{max} in each of these two steels is lower than in its binary analogue by about three times. For the nucleation stage, the precipitates density $d_p(t)$ and their mean size $R(t)$ observed in [6] in the NUCu-140 steel seem to be close to those simulated for the Fe–1.17Cu alloy, contrary to the case of the NUCu-170 steel, for which the $d_p(t)$ and $R(t)$ values at $t = 0.25$ h reported in [5] sharply disagree with those simulated for the Fe–1.82Cu alloy. In this connection, we note that the $R(0.25\mathrm{h}) = R_{\mathrm{KS}}$ value reported in [5] seems to be unrealistically large for the early nucleation stage supposed in [5] for the NUCu-170 steel at $t = 0.25$ h: $R_{\mathrm{KS}} \approx 4R_c$. Therefore, further experimental studies of the nucleation kinetics in Fe–Cu-based steels seem to be desirable.

For the coarsening stage, the presence of alloying elements in the NUCu steels leads to a very strong slowing down of coarsening, by 1 to 2 orders of magnitude, compared with their binary analogues. A similar strong slowing down of coarsening was also observed in [4] for an irradiated ternary Fe–Cu–Mn alloy. At the same time, for the nucleation and growth stages, the effects of the alloying elements on the maximum precipitate density d_{max} in the NUCu steels and in the Fe–Cu–Mn alloy studied in [7] seem to be qualitatively different. Some hypotheses about a possible origin of the universal slowing down of coarsening in multicom-

ponent Fe–Cu-based alloys with respect to their binary analogues are suggested.

We are very grateful to F. Soisson for providing us with the kinetic Monte Carlo codes used for all KMC simulations in this paper, as well as for the valuable critical remarks. We are also much indebted to Dr. R. Shabadi for sending a preprint of paper [7] prior to publication. The work was supported by the Russian Foundation of Basic Research (grant No. 12-02-00093), by the Fund for Support of Leading Scientific Schools of Russia (grant No. NS-215.2012.2), and by the Program of Russian University Scientific Potential Development (grant No. 2.1.1/4540).

REFERENCES

1. S. R. Goodman, S. S. Brenner, and J. R. Low, Metall. Trans. **4**, 2363, 2371 (1973).
2. R. Kampmann and R. Wagner, in: *Atomic Transport and Defects in Metals by Neutron Scattering*, ed. by C. Janotet et al., Springer, New York (1986), p. 73.
3. M. H. Mathon, A. Barbu, F. Dunstetter, F. Maury, N. Lorenzelli, and C. H. de Novion, J. Nucl. Mater. **245**, 224 (1997).
4. M. K. Miller, B. D. Wirth, and G. R. Odette, Mater. Sci. Eng. **353**, 133 (2003).
5. R. P. Kolli and D. N. Seidman, Acta Mater. **56**, 2073 (2008).
6. R. P. Kolli, R. M. Wojes, S. Zaucha, and D. N. Seidman, Int. J. Mat. Res. **99**, 513 (2008).
7. R. Shabadi, R. Taillard, B. Radiget, J. De Baerdemaeker, and E. Leunis, Sol. St. Phen. **172–174**, 297 (2011).
8. F. Soisson, J. Nucl. Mater. **349**, 235 (2006).
9. F. Soisson and C.-C. Fu, Phys. Rev. B **76**, 214102 (2007).
10. F. Soisson and C.-C. Fu, Sol. St. Phen. **139**, 107 (2008).
11. F. Soisson, C. Becquart, N. Castin, C. Domain, L. Malerba, and E. Vincent, J. Nucl. Mater. **406**, 55 (2010).
12. A. Yu. Stroev, I. R. Pankratov, and V. G. Vaks, Phys. Rev. B **77**, 134203 (2008).
13. K. Yu. Khromov, F. Soisson, A. Yu. Stroev, and V. G. Vaks, JETP **112**, 415 (2011).
14. V. Yu. Dobretsov and V. G. Vaks, J. Phys.: Condensed Matter **10**, 2261, 2275 (1998).
15. V. G. Vaks, I. A. Zhuravlev, and K. Yu. Khromov, Zh. Exp. Teor. Fiz. **138**, 902 (2010).
16. V. G. Vaks and K. Yu. Khromov, Zh. Exp. Teor. Fiz. **133**, 115 (2008).
17. K. Yu. Khromov, V. G. Vaks, and I. A. Zhuravlev, http://arxiv.org/abs/1206.1792v1.
18. V. G. Vaks and I. A. Zhuravlev, Zh. Exp. Teor. Fiz. **142** (2012), in press; http://arxiv.org/abs/1201.6056.
19. M. Nastar, V. Yu. Dobretsov, and G. Martin, Phil. Mag. A **80**, 155 (2000).
20. F. Soisson and G. Martin, Phys. Rev. B **62**, 203 (2000).
21. A. V. Barashev, S. I. Golubov, D. J. Bacon, P. E. J. Flewitt, and T. A. Lewis, Acta Mater. **52**, 877 (2004).
22. I. M. Lifshits and V. V. Slyozov, J. Phys. Chem. Sol. **19**, 35 (1961).
23. C. Z. Wagner, Electrochem. **65**, 581 (1961).